Space Weather

RESEARCH ARTICLE
10.1029/2023SW003683

Calculating the High-Latitude Ionospheric Electrodynamics Using a Machine Learning-Based Field-Aligned Current Model

V. Sai Gowtam[1], Hyunju Connor[2], Bharat S. R. Kunduri[3], Joachim Raeder[4], Karl M. Laundal[5], S. Tulasi Ram[6], Dogacan S. Ozturk[1], Donald Hampton[1], Shibaji Chakraborty[3], Charles Owolabi[1], and Amy Keesee[4]

[1]Geophysical Institute, University of Alaska Fairbanks, Fairbanks, AK, USA, [2]Goddard Space Flight Center, NASA, Greenbelt, MD, USA, [3]Virginia Tech, Blacksburg, VA, USA, [4]University of New Hampshire, Durham, NH, USA, [5]Department of Physics and Technology, University of Bergen, Bergen, Norway, [6]Indian Institute of Geomagnetism, Navi Mumbai, India

Abstract We introduce a new framework called Machine Learning (ML) based Auroral Ionospheric electrodynamics Model (ML-AIM). ML-AIM solves a current continuity equation by utilizing the ML model of Field Aligned Currents of Kunduri et al. (2020, https://doi.org/10.1029/2020JA027908), the FAC-derived auroral conductance model of Robinson et al. (2020, https://doi.org/10.1029/2020JA028008), and the solar irradiance conductance model of Moen and Brekke (1993, https://doi.org/10.1029/92gl02109). The ML-AIM inputs are 60-min time histories of solar wind plasma, interplanetary magnetic fields (IMF), and geomagnetic indices, and its outputs are ionospheric electric potential, electric fields, Pedersen/Hall currents, and Joule Heating. We conduct two ML-AIM simulations for a weak geomagnetic activity interval on 14 May 2013 and a geomagnetic storm on 7–8 September 2017. ML-AIM produces physically accurate ionospheric potential patterns such as the two-cell convection pattern and the enhancement of electric potentials during active times. The cross polar cap potentials (Φ_{PC}) from ML-AIM, the Weimer (2005, https://doi.org/10.1029/2004ja010884) model, and the Super Dual Auroral Radar Network (SuperDARN) data-assimilated potentials, are compared to the ones from 3204 polar crossings of the Defense Meteorological Satellite Program F17 satellite, showing better performance of ML-AIM than others. ML-AIM is unique and innovative because it predicts ionospheric responses to the time-varying solar wind and geomagnetic conditions, while the other traditional empirical models like Weimer (2005, https://doi.org/10.1029/2004ja010884) designed to provide a quasi-static ionospheric condition under quasi-steady solar wind/IMF conditions. Plans are underway to improve ML-AIM performance by including a fully ML network of models of aurora precipitation and ionospheric conductance, targeting its characterization of geomagnetically active times.

Plain Language Summary Auroral ionospheric electrodynamics, originating from the interaction of solar wind with Earth's magnetosphere-ionosphere system, is vital in space weather forecasting, as it influences satellite communication, satellite drag, navigation, and power distribution systems on Earth. Machine learning (ML), a subset of artificial intelligence, has demonstrated considerable potential within the realm of space weather research, yielding promising outcomes for forecasting operations. In this work, we have developed a new ML-based auroral ionospheric electrodynamics model (ML-AIM) by extending an existing ML-based model for ionospheric currents. ML-AIM uses 60-min time history of solar and geomagnetic input conditions to nowcast the ionospheric electrodynamics. The present model is capable of better representing the ionospheric response to the time-varying solar input conditions. This work laid a successful groundwork for integrating various advanced ML models within a single framework to accurately model the space weather relevant quantities.

Key Points:

- ML-AIM predicts high-latitude ionospheric electrodynamics based on 1-hr time histories of SW/IMF conditions and geomagnetic indices
- ML-AIM performs better in predicting cross polar cap potentials than the Weimer (2005) and SuperDARN data-assimilated models
- ML-AIM considers gradual ionospheric responses to consistently varying SW/IMF conditions, unlike traditional empirical models

Correspondence to:
V. S. Gowtam,
gowtham.physics12@gmail.com

Citation:
Gowtam, V. S., Connor, H., Kunduri, B. S. R., Raeder, J., Laundal, K. M., Tulasi Ram, S., et al. (2024). Calculating the high-latitude ionospheric electrodynamics using a machine learning-based field-aligned current model. *Space Weather*, *22*, e2023SW003683. https://doi.org/10.1029/2023SW003683

Received 15 AUG 2023
Accepted 24 MAR 2024

Author Contributions:
Conceptualization: V. Sai Gowtam, Hyunju Connor
Data curation: V. Sai Gowtam, Hyunju Connor, Bharat S. R. Kunduri, Karl M. Laundal, Dogacan S. Ozturk, Shibaji Chakraborty, Charles Owolabi
Formal analysis: V. Sai Gowtam, Hyunju Connor, Bharat S. R. Kunduri, Joachim Raeder, Karl M. Laundal, Dogacan S. Ozturk, Donald Hampton, Charles Owolabi, Amy Keesee
Funding acquisition: Hyunju Connor, Amy Keesee
Investigation: V. Sai Gowtam, Hyunju Connor, S. Tulasi Ram, Donald Hampton, Charles Owolabi
Methodology: V. Sai Gowtam, Hyunju Connor, Bharat S. R. Kunduri, Joachim Raeder, Karl M. Laundal, S. Tulasi Ram, Dogacan S. Ozturk, Amy Keesee

1. Introduction

The global specification of the high latitude ionospheric electrodynamics plays a crucial role in analyzing space weather impacts and mitigating the threats posed by space weather events on humans and technological systems. The Field Aligned Currents (FACs) (Birkeland current system; Birkeland, 1901) flow along the Earth's magnetic field lines and electrodynamically couple the magnetosphere and ionosphere. The FACs consist of two large current systems, known as Region 1 (R1) and Region 2 (R2) currents. The R1 currents in the dawn (dusk) sector

Project administration: Hyunju Connor, Donald Hampton, Amy Keesee
Resources: V. Sai Gowtam, Hyunju Connor
Software: V. Sai Gowtam, Hyunju Connor, Bharat S. R. Kunduri, Joachim Raeder, Karl M. Laundal, Dogacan S. Ozturk, Shibaji Chakraborty
Supervision: Hyunju Connor, Bharat S. R. Kunduri, Joachim Raeder, Donald Hampton, Amy Keesee
Validation: V. Sai Gowtam, Hyunju Connor, Joachim Raeder, Karl M. Laundal, S. Tulasi Ram, Dogacan S. Ozturk, Charles Owolabi, Amy Keesee
Visualization: V. Sai Gowtam, Hyunju Connor, Dogacan S. Ozturk, Shibaji Chakraborty
Writing – original draft: V. Sai Gowtam, Hyunju Connor
Writing – review & editing: V. Sai Gowtam, Hyunju Connor, Bharat S. R. Kunduri, Joachim Raeder, Karl M. Laundal, S. Tulasi Ram, Dogacan S. Ozturk, Donald Hampton, Shibaji Chakraborty, Charles Owolabi, Amy Keesee

flow into (out of) the ionosphere at the latitude close to the poles in the auroral region, whereas the R2 currents in the dawn (dusk) sector flow out of (into) the ionosphere at the equatorward part of the auroral oval (Iijima & Potemra, 1976). As a response to the electrodynamic coupling between the magnetosphere and ionosphere, the horizontal flow of ionospheric currents (Pedersen and Hall currents) can be noticed in the auroral region (Richmond & Thayer, 2000). During disturbed space weather periods, the FACs, plasma convection, and the horizontal currents over the auroral region are significantly altered. These enhanced horizontal currents are associated with large geomagnetic field perturbations (Pirjola, 2005) on the ground, which can potentially damage the power grids (Pulkkinen & Engels, 2005; Pulkkinen et al., 2013). Further, enhanced particle precipitation at higher latitudes increases the conductivity of the ionosphere, modifying ionospheric electric field, plasma convection, and Joule heating patterns in a complex way that alters the thermospheric temperature and density (Blanc & Richmond, 1980). As a result, many satellites and space debris in the Low Earth Orbit can be subjected to increased atmospheric drag. Therefore, understanding and accurately characterizing the high latitude ionosphere are essential for space weather applications.

Significant progress has been made over the past several decades in predicting high-latitude ionospheric electrodynamics through data-driven and physics-based modeling techniques. By utilizing a large set of space/ground observations, empirical models parameterize various ionospheric properties under different solar wind/IMF conditions: for example, mean energy and total energy flux of precipitating particles (Fuller-Rowell & Evans, 1987; Hardy et al., 1987; Newell et al., 2009, 2014), electrostatic potentials, electric fields, Joule heating rate and FACs (Heelis et al., 1982; Ruohoniemi & Greenwald, 1996; Thomas & Shepherd, 2018; Weimer, 2005), Pedersen and Hall conductance (Moen & Brekke, 1993; Robinson et al., 1987), and auroral ionospheric currents (Laundal et al., 2018). Physics-based models also solve global ionospheric electrodynamics by considering the ionosphere—thermosphere dynamics—for example, Thermosphere-Ionosphere-Mesosphere-Electrodynamics General Circulation Model (TIMEGCM, Roble & Emery, 1983), and Global Ionosphere Thermosphere Model (GITM, Ridley et al., 2006), by coupling a global magnetosphere model with the ionosphere—thermosphere model—for example, Global Geospace Environment Modeling-Coupled Thermosphere Ionosphere Model (OpenGGCM-CTIM; Connor et al., 2014; Fuller-Rowell et al., 1996; Raeder et al., 2001), using diverse types of measurements - for example, Assimilative Mapping of Ionosphere Electrodynamics model (Lu et al., 1996; Richmond & Kamide, 1988) and by assimilating the model predictions with space/ground observations—for example, Assimilative Mapping of Geospace Observations (AMGeO; Matsuo et al., 2019).

The physics-based models are better at resolving magnetospheric processes that contribute to ionospheric electrodynamics (Connor et al., 2016) compared to empirical formulation; however, these models require large computational resources. The empirical models (e.g., Thomas & Shepherd, 2018; Weimer, 2005) are designed to predict an average state of the ionospheric parameters for various solar wind conditions in a computationally efficient manner. However, these statistical models are unable to predict the temporal evolution of ionospheric electrodynamics under consistently varying SW/IMF conditions. For example, when Interplanetary Magnetic Field (IMF) Bz turns from positive to negative, these models indicate an instantaneous transition from a quiet to an active ionospheric state without considering a time for the ionosphere to adjust to the new driving conditions. Rastaetter et al. (2016) carried out a comprehensive validation of empirical and theoretical models during six selected geomagnetic events and concluded that the convection electric fields or Poynting flux and the timing of the system responses are not captured in any of the existing empirical and the physics-based models. Due to the complex and dynamic coupling between the solar wind and the Magnetosphere-Ionosphere-Thermosphere (M-I-T) system, predicting the auroral ionosphere electrodynamics is still a challenging task for the scientific community. More work should be done in developing new ionospheric electrodynamics models for accurately parameterizing the high-latitude sources and for predicting various ionosphere-thermosphere quantities.

Recently, Machine Learning (ML) and artificial intelligence has shown promising results in M-I-T system modeling (Blandin et al., 2022; Bristow et al., 2022; Gowtam et al., 2019; Hu et al., 2022; Kunduri et al., 2020; Liu et al., 2020; McGranaghan et al., 2021; Pinto et al., 2022; Sai Gowtam & Tulasi Ram, 2017; Tulasi Ram et al., 2018 and references therein). The ML models require large data sets to learn the relationship between inputs and outputs through systematic learning processes. Further, the training process requires moderate to large computational resources. However, the use of ML models after training does not require large computational power and can be easily run with personal computers. The main aim of this paper is to take advantage of such advanced ML models to develop a new ML-based Auroral Ionospheric electrodynamics Model (hereafter, ML-AIM). The ionospheric electrodynamics can be derived from ionospheric Ohm's law if we explicitly know the

conductance and if we also know either FACs, electric fields, horizontal currents, background neutral winds or magnetic field perturbations (using Biot-Savart law). In this study, we apply recent results from an ML-based FAC model by Kunduri et al. (2020) and an empirical specification of auroral conductance by Robinson et al. (2020) to get the potential pattern and other electrodynamic parameters in the ML-AIM framework.

The organization of the paper is as follows. In Section 2, we describe the methodology and ML-AIM framework used to derive the ionospheric electrodynamics. Section 3 describes the data sets used in the study for validating the ML-AIM. Section 4 presents the case studies of the ML-AIM response to the varying solar and geomagnetic inputs. Section 5 discusses the ML-AIM advantages and shortcomings. Section 6 provides a summary and the scope of future work.

2. Methodology

2.1. Deep Convolution Neural Network-Based Field Aligned Current Model (CNN-FAC)

The Active Magnetosphere and Planetary Electrodynamics Response Experiment (AMPERE) provides global maps of the FACs from magnetic field perturbations measured by the Iridium constellation of 66+ commercial satellites at ∼780-km polar circular orbits (Anderson et al., 2000, 2002, 2014; Waters et al., 2020). The magnetic field perturbations are processed by removing the background International Geomagnetic Reference Field and long-period residuals from the observations (Anderson et al., 2000) to determine FAC densities. Recently, Kunduri et al. (2020) developed a deep learning-based convolutional neural network model of FACs (hereinafter referred to as CNN-FAC) by utilizing nearly 7 years (2010–2016) of AMPERE FAC data. The CNN-FAC input parameters are 60-min time histories of IMF components (B_x, B_y, and B_z), solar wind velocity (V_x), proton number density (N_p), geomagnetic indices (Sym-H, Asym-H, SuperMAG AL, and AU indices), F10.7 solar flux, and the month number. The output parameters are the global pattern of Birkeland currents in the Northern Hemisphere at a given time. Kunduri et al. (2020) compared the CNN-FAC model results with the bin-averaged statistical pattern under steady and time-varying input conditions. The CNN-FAC model successfully reproduced prominent current systems, such as R1 and R2 FACs, the NBZ current system, and the cusp currents. Furthermore, Kunduri et al. (2020) showed that the CNN-FAC model accurately captured the time evolution of Birkeland currents under varying solar and geomagnetic conditions. Therefore, we adopted the CNN-FAC model by Kunduri et al. (2020) in our ML-AIM framework to compute the FACs.

2.2. Ionospheric Conductance Model

Solar Irradiance and auroral precipitation are key factors that determine ionospheric conductance. Moen and Brekke (1993) provided empirical equations of height-integrated Pedersen and Hall conductance (Σ_P and Σ_H) caused by solar irradiance:

$$\Sigma_{P_{Solar}} = F_{10.7}^{0.49}\left(0.34\cos\chi + 0.93\,cos^{1/2}\chi\right) \quad (1)$$

$$\Sigma_{H_{Solar}} = F_{10.7}^{0.53}\left(0.81\cos\chi + 0.54\,cos^{1/2}\chi\right) \quad (2)$$

where F10.7 is the solar radio flux at 10.7 cm and χ is the solar zenith angle. Robinson et al. (2020) introduced new empirical equations of ionospheric conductance caused by auroral precipitation. They first derived the height-integrated ionospheric conductance from the Poker Flat Incoherent Scatter Radar (PFISR) observations for 20 geomagnetically disturbed days. Then, they compared the conductance data with the AMPERE FACs over PFISR during the same disturbed days, and established a linear relationship between the height-integrated conductance and FACs for 8 magnetic local time (MLT) zones:

$$\Sigma_{P_{Aurora}} = \Sigma_{P0}^{U} + \Sigma_{P1}^{U} j_{\parallel}\ \left(j_{\parallel} > 0\right) \quad (3)$$

$$\Sigma_{P_{Aurora}} = \Sigma_{P0}^{D} + \Sigma_{P1}^{D} j_{\parallel}\ \left(j_{\parallel} < 0\right) \quad (4)$$

$$\Sigma_{H_{Aurora}} = \Sigma_{H0}^{U} + \Sigma_{H1}^{U} j_{\parallel}\ \left(j_{\parallel} > 0\right) \quad (5)$$

$$\Sigma_{H_{Aurora}} = \Sigma_{H0}^{D} + \Sigma_{H1}^{D} j_{\parallel}\ \left(j_{\parallel} < 0\right) \quad (6)$$

where the superscripts U and D indicate upward and downward FAC regions, respectively. Each coefficient —Σ^U_{P1}, Σ^U_{H1}, Σ^D_{P1}, Σ^D_{H1}, Σ^U_{P0}, Σ^U_{H0}, Σ^D_{P0}, and Σ^D_{H0}—is different for each MLT sector and obtained from Table 1 of Robinson et al. (2020). Robinson et al. (2021) utilized these new conductance equations in Robinson et al. (2020) to derive ionospheric potentials, Hall/Pedersen currents, ground geomagnetic field perturbations, and auroral indices (e.g., AU, AL, and AE). Their results showed good agreement with the SuperMAG geomagnetic indices. Therefore, our ML-AIM framework adopts the auroral conductance model of Robinson et al. (2020) along with the solar irradiance conductance model of Moen and Brekke (1993) to derive the Pedersen and Hall conductances. The conductance in ML-AIM framework is given by,

$$\Sigma_P = \left(\Sigma^2_{P_{Solar}} + \Sigma^2_{P_{Aurora}}\right)^{1/2} \tag{7}$$

$$\Sigma_H = \left(\Sigma^2_{H_{Solar}} + \Sigma^2_{H_{Aurora}}\right)^{1/2} \tag{8}$$

The quadratic addition is employed due to the fact that the ionization rate below 200 km is directly proportional to the square of the electron density (Robinson et al., 2020). Therefore, Equations 7 and 8 serve as approximations to the altitude-dependent cumulative ionization production rates resulting from auroral precipitation and solar illumination.

2.3. High-Latitude Ionospheric Electrodynamics Model

ML-AIM defines a high-latitude ionosphere as a 2D planar ionosphere and calculates ionospheric potential assuming that FACs generated from the solar wind—magnetosphere interaction are closed in the ionosphere (Raeder, 2003; Raeder et al., 1998, 2001). Under this assumption, high-latitude electrodynamics can be expressed by the current continuity equation and the ionospheric Ohm's law (Goodman, 1995; Wolf, 1983):

$$j_{\parallel} = -\nabla.\bar{j}_{\perp} = -\nabla\,.\,\bar{\bar{\Sigma}}\bar{E} \tag{9}$$

$$\bar{E} = -\nabla\phi \tag{10}$$

where $j_{\parallel}$ is the FAC density, $\bar{J}_{\perp}$ is the horizontal current density, $\bar{\bar{\Sigma}}$ is the conductance tensor, $\bar{E}$ is the electric field, and Φ is the electrostatic potential. It is important to mention the assumptions involved in the above formulation. The ionospheric Ohm's law applies when there is a force balance between Lorentz forces and collisions with neutrals. It also assumes that the neutral winds are almost absent in the corotating frame. Further, it is assumed that the electric fields are curl free.

The conductivity tensor in the above equation is given by,

$$\bar{\bar{\Sigma}} = \begin{pmatrix} \Sigma_{\theta\theta} & \Sigma_{\theta\lambda} \\ -\Sigma_{\theta\lambda} & \Sigma_{\lambda\lambda} \end{pmatrix} \tag{11}$$

$$\Sigma_{\theta\theta} = \frac{\Sigma_P}{\sin^2 I} \quad , \quad \Sigma_{\theta\lambda} = \frac{\Sigma_H}{\sin I} \quad , \quad \Sigma_{\lambda\lambda} = \Sigma_P \tag{12}$$

where θ is the magnetic latitude (MLAT), λ is the magnetic longitude, and I is the inclination of the magnetic field lines. We derived the high latitude potential patterns by solving Equations 9–12 with the FACs and ionospheric conductance obtained from the models in Sections 2.1 and 2.2.

Figure 1 summarizes four important steps in the ML-AIM framework. In step 1, the solar and geomagnetic inputs with a 1-min time resolution are prepared for the model run. In step 2, the FACs are computed using the CNN-FAC model of Kunduri et al. (2020). In step 3, the solar irradiance conductance maps are generated using the empirical formulation of Moen and Brekke (1993), while the auroral conductance maps are computed using the empirical relationship of Robinson et al. (2020) with the ML prediction of FACs. In step 4, the current continuity Equation 9 is solved to get the ionospheric electrostatic potentials, electric field, horizontal currents, and Joule heating rates. We used the ionospheric potential solver developed as part of the OpenGGCM-CTIM model (Raeder et al., 2001) for solving Equations 9–12.

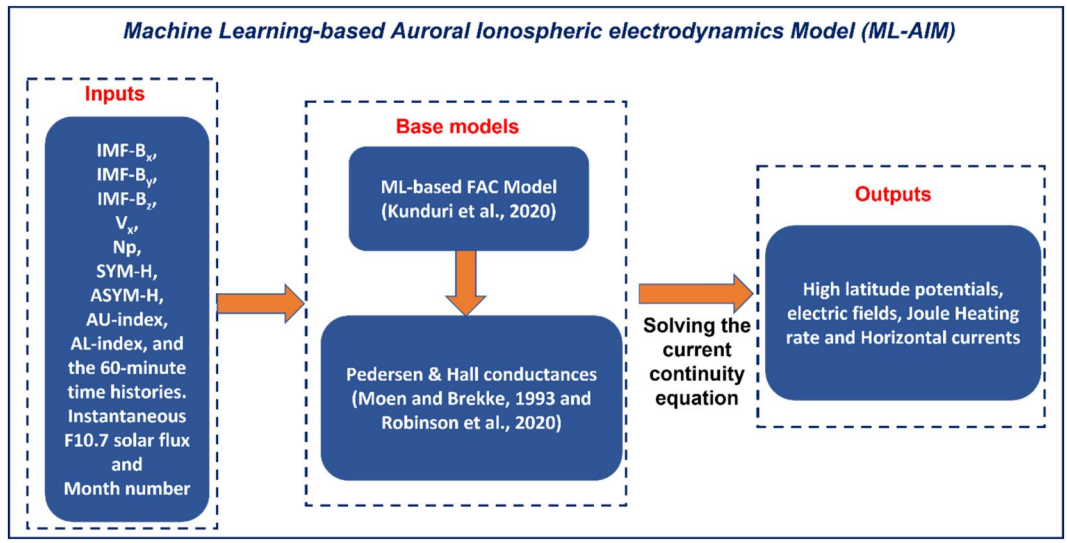

Figure 1. Block diagram of Machine Learning based Auroral Ionosphere Model (ML-AIM).

3. Data Sets

We used the Defense Meteorological Satellite Program (DMSP) ionospheric flow measurements and the cross polar cap potential (CPCP; Φ_{PC}) derived from the DMSP data for comparing the ML-AIM results. We select the F17 spacecraft since its dawn-dusk orbit provides optimal coverage of typical two-cell ionospheric convection patterns and thus its data are well-suited for the Φ_{PC} calculation. We downloaded the DMSP F17 data from the Madrigal Database at Cornell (http://landau.geo.cornell.edu/madrigal/) and estimated Φ_{PC} by following the method of Boudouridis et al. (2005). Considering the frozen-in flux conditions in the topside ionosphere, the electric field along the satellite trajectory is expressed as:

$$E_x = -V_y \cdot B_z + V_z \cdot B_y \tag{13}$$

Here, $+x$ is parallel to the spacecraft velocity vector, $+z$ is upward away from Earth and $+y$ completes a right-handed coordinate system. For dawn-dusk orbits of DMSP F17, $+y$ mainly points toward the Sun, making E_x close to the dawn-dusk electric field. Then, the electrostatic potential can be computed by integrating electric fields along the satellite path l (Rich & Hairston, 1994),

$$\phi(l) = \int_{l_1}^{l_2} (E_x - E_{cor})\, dl \approx \sum_{l_1}^{l_2} E_x \Delta l \tag{14}$$

where l_1 and l_2 are dawn and dusk-side reference points on the satellite trajectory and are defined to have zero electric potential. Here, it is assumed that all the electric fields measured by DMSP are static electric fields; there is no inductive electric field from dB/dt. The initial point of integration, denoted as $l1$, is chosen at a subauroral latitude. In this region, excluding corotation, both horizontal and vertical ion flows remain constant or close to zero (usually around 50°–60° MLAT in the dawn sector). The end point, labeled as $l2$, is similarly chosen, and is usually positioned at around 50°–60° MLAT in the dusk sector. Typically, $\phi(l)$ calculated from the l_1 point along the DMSP orbit gives a non-zero value at l_2, which is called potential offset (ϕ_{offset}). We adjusted $\phi(l)$ to remove this offset at l_2—that is, to make zero potential at l_2—using the linear correction method of Boudouridis et al. (2005):

$$\phi_{corrected}(l) = \phi_{measured}(l) - \phi_{offset} \cdot \left(\frac{l - l_1}{l_2 - l}\right) \tag{15}$$

Finally, we obtain Φ_{PC} by calculating the difference between the maximum and minimum values of $\phi_{corrected}$. The DMSP Φ_{PC} is an observation-based parameter and can be considered as ground truth for model validation (e.g., Connor et al., 2014). However, Φ_{PC} includes some errors and requires caution when comparing the model results. First, the DMSP F17 orbit may miss real maximum/minimum potential regions in the northern ionosphere, and thus Φ_{PC} may be underestimated. Second, ionospheric potential patterns may change during 20–25 min of the DMSP path over the northern polar ionosphere, and thus the DMSP Φ_{PC} may include a large error, especially during an active time.

We also used the ionospheric potentials and Φ_{PC} obtained from the Weimer 2005 model (Weimer, 2005) and the SuperDARN Assimilative Mapping procedure (e.g., Cousins & Shepherd, 2010; Cousins et al., 2013; Thomas & Shepherd, 2018) to compare with the ML-AIM results. The Weimer (2005) results are generated by using the run-on-request service of the Community Coordinated Modeling Center (CCMC; https://ccmc.gsfc.nasa.gov/). The SuperDARN potentials are generated by optimally combining SuperDARN observations and a statistical convection model of Thomas and Shepherd (2018). We calculate the Φ_{PC} of Weimer (2005) and SuperDARN by using the difference between maximum and minimum values of the global ionospheric electric potential maps.

4. Results

4.1. ML-AIM Response to the Weak Geomagnetic Activity

To demonstrate the methodology explained in the previous sections, we have run ML-AIM for a weak geomagnetic activity period on 14 May 2013. We highlighted the SW/IMF condition used to generate Figure 2. A vertical dashed line and a shaded area in Figure 3 indicate the prediction time used in Figure 2 (i.e., 12:44UT) and the corresponding input period for the prediction (i.e., 11:44–12:44 UT), respectively. Figure 2a shows the MLT and MLAT map of the FACs at 12:44 UT generated by the CNN-FAC model with 1 hr time history of solar wind and geomagnetic indices (i.e., 11:44–12:44 UT) as input. The prediction time at 12:44 UT and the corresponding input period for the prediction (11:44–12:44 UT) are displayed as a vertical dashed line and a shaded area in Figure 3, respectively. The positive and negative values in Figure 2a indicate the upward and downward flow of the FACs, respectively. The Birkeland currents are clearly observed with the downward (upward) FACs in the dawn (dusk) sector at higher latitudes, that is, region 1 currents, and the upward (downward) FACs in the dusk (dawn) sectors at lower latitudes, that is, region 2 currents. Figures 2b and 2c display the Pedersen and Hall conductances calculated from Equations 1–6 with the FAC input from Figure 2a. Both Pedersen and Hall conductances are enhanced at the regions of large FACs, as expected by the empirical conductance Equations 3–6.

ML-AIM computes the electrostatic potential by solving Equations 9–12 with a boundary condition of zero potential at 40° MLAT. Figure 2d shows MLAT and MLT distribution of the electrostatic potential calculated from the FACs and ionospheric conductance in Figures 2a–2c. When IMF Bz turns from north to south, the plasma in the polar cap undergoes a circulation, in which the opening and closing of Earth's magnetic flux leads to an anti-sunward motion of plasma across the high-latitude regions and sunward return flow at low latitudes, known as the “Dungey cycle” (Dungey, 1961). This creates a well-known two-cell convection pattern of the high latitude potential. ML-AIM reproduces this convection pattern with maximum potential in the dawn sector and minimum potential in the dusk sector. We also plotted horizontal plasma flows, observed by DMSP F17 with the magenta lines in Figure 2d. When the DMSP F17 crosses near the maximum or minimum potential region, flow reversals are expected in the in situ observations. The DMSP velocity reversal point in the morning sector matches well with the ML-AIM maximum potential region, while in the afternoon sector, the velocity turning point is slightly off from the minimum potential region. The ML-AIM Φ_{PC} of 63 kV is comparable to the DMSP Φ_{PC} of 59 kV for this period (see the upper right corner of Figure 2d). Figures 2e and 2f show the Joule heating rate and the Hall currents, respectively. As expected, the Joule heating rate and Hall currents enhance in the regions where both FACs (Figure 2a) and conductances (Figures 2b and 2c) are strong.

Figure 3 compares Φ_{PC} of various models and DMSP observations during the entire period of this event on 14 May 2013. Figures 3a–3c show IMF, solar wind velocity, and number density in the Geocentric Solar Magnetospheric coordinates, respectively. IMF B_z turned southward after 6:50 UT and it was steadily southward until 20:50 UT except for a short period of northward IMF during ∼17:40–19:05 UT. Figure 3d shows Φ_{PC} calculated every 2 min using ML-AIM (blue), Weimer (2005) (green), and SuperDARN fitted Potentials (orange) as well as Φ_{PC} computed from the DMSP observations (magenta dots) during the satellite crossings over the northern hemisphere (magenta bars). Overall, Φ_{PC} patterns of ML-AIM, Weimer (2005), and SuperDARN models are

10.1029/2023SW003683

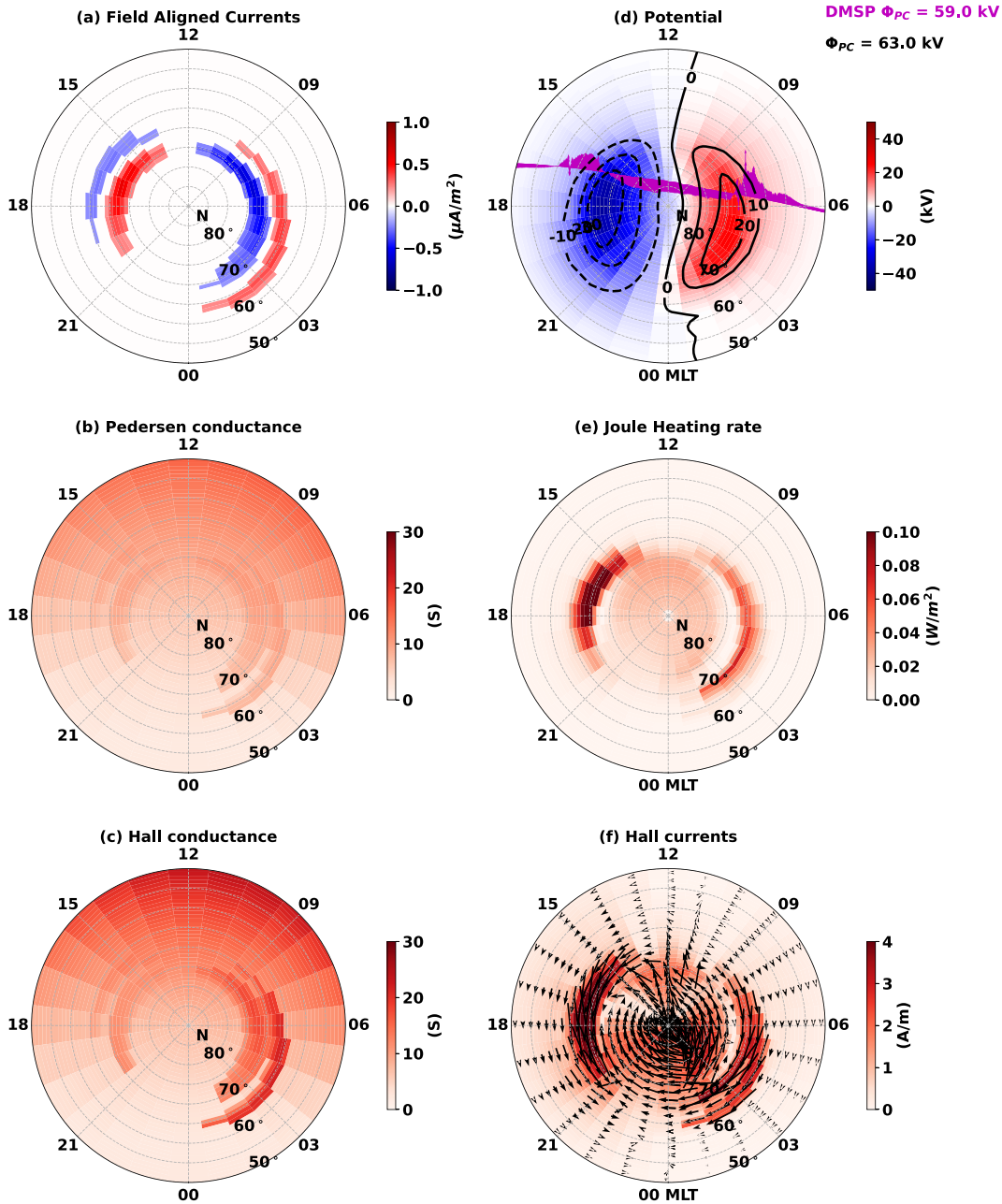

Figure 2. Magnetic Local Time (MLT) and Magnetic Latitude (MLAT) maps of (a) Field Aligned Current densities, (b) Pedersen conductance, (c) Hall conductance, (d) potential, (e) Joule heating rate, and (f) magnitude and directions (black arrows) of Hall currents at 12:44 UT on 14 May 2013. The noon is located at the top of each plot. The dashed gray lines indicate a grid of 3 hr MLT and 5° MLAT, respectively. Solar wind/Interplanetary Magnetic Field conditions are shown with dashed vertical line in Figure 3.

similar to each other, with the Weimer (2005) model providing the highest Φ_{PC} almost always. All the modeled Φ_{PC} increases during southward IMF and decreases during northward IMF, showing a good agreement with the DMSP Φ_{PC}. However, it is interesting to note that ML-AIM Φ_{PC} responds slowly to the sharp changes of IMF Bz at 6:50 and 20:50 UT, while Φ_{PC} of Weimer (2005) and SuperDARN potential models responds immediately. Section 5 discusses this behavior in detail. Figures 2 and 3 suggest that the ML-AIM framework successfully reproduced the general morphological features of the auroral electrodynamics during a period of weak geomagnetic activity.

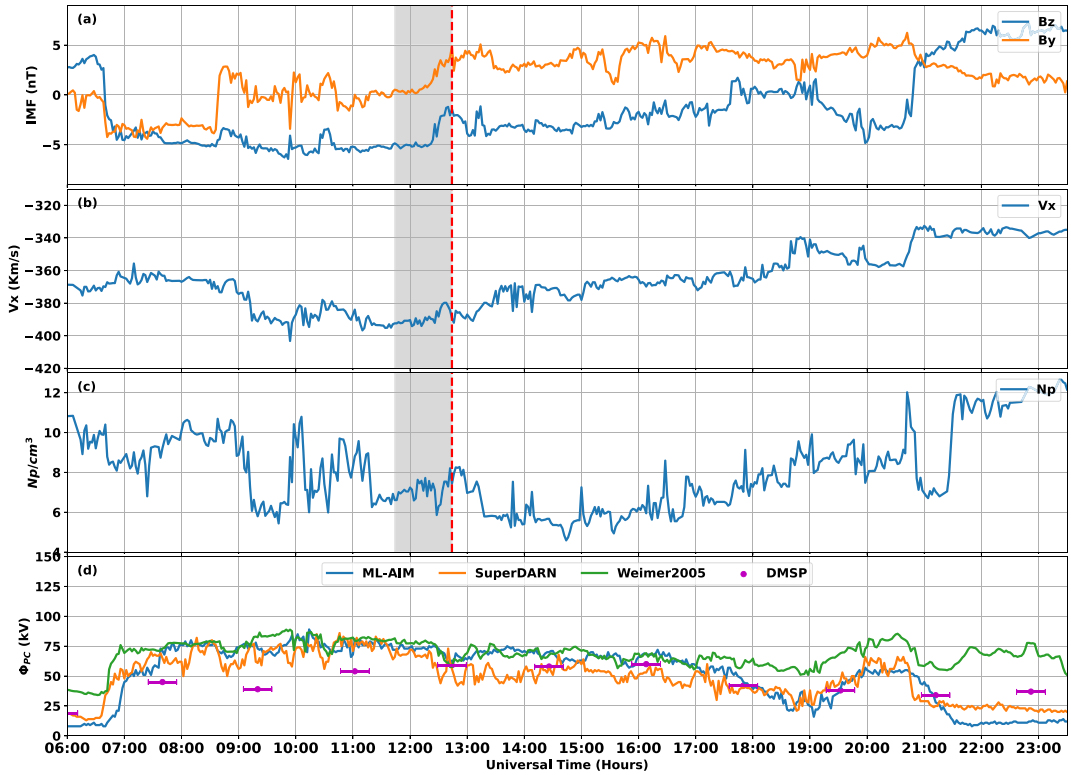

Figure 3. (a) IMF B_y and B_z, (b) solar wind velocity Vx in the Geocentric Solar Magnetospheric coordinates, and (c) number density obtained from the NASA OMNI data during 14 May 2013. The bottom panel shows the cross polar cap potential drop (Φ_{PC}) of the northern hemisphere predicted by the ML-AIM (blue), Weimer (2005) (green), and SuperDARN potential models (orange). Magenta circles indicate the Φ_{PC} calculated from each polar crossing of Defense Meteorological Satellite Program (DMSP) F17. Time taken for each polar crossing of DMSP is indicated using the horizontal magenta bars. A vertical dashed line and a shaded area indicate the prediction time used in Figure 2 (i.e., 12:44UT) and the corresponding input period for the prediction (i.e., 11:44–12:44 UT), respectively.

4.2. ML-AIM Response to a Geomagnetic Storm During 7–8 September 2017

A geomagnetic storm on 7–8 September 2017 is selected for studying the ML-AIM response to strong geomagnetic disturbances. An X9.3 class solar flare and associated coronal mass ejection occurred on 6 September 2017 and triggered a global geomagnetic storm on the following days. Figure 4 shows IMF, solar wind velocity, number density, and SYM-H index from top to bottom with 1-min time resolution during 7–8 September 2017. IMF Bz turned southward soon after 20:30 UT and stayed southward for ∼5.5 hr with a minimum value of −31 nT at ∼23:30UT on 7 September 2017, when solar wind velocity and density also increased. The SYM-H index reached its minimum value of −146 nT around 01:08 UT on 8 September 2017, and a storm recovery started after the northward turning of IMF Bz at ∼02:00 UT on 8 September 2017. However, SYM-H decreased again as IMF Bz turned southward at ∼11:40 UT on 8 September 2017 and the storm recovery continued till 9 September 2017.

Figure 4e shows Φ_{PC} of the northern hemisphere predicted by ML-AIM (blue), Weimer (2005) (green), and SuperDARN (orange) potential maps. Magenta dots and bars indicate the DMSP Φ_{PC} and the DMSP observation intervals used for the Φ_{PC} calculations. The vertical dashed gray lines indicate three incidents used for deeper analysis in Figure 5. As SYM-H started decreasing after 20:30 and 11:00 UT, all three models showed Φ_{PC} enhancement, similar to the DMSP observations. However, ML-AIM Φ_{PC} responded more smoothly to the rapid IMF Bz fluctuations than the other two empirical models. For example, the Weimer (2005) and SuperDARN models showed rapid Φ_{PC} reduction soon after the short excursions to northward IMF near 20:30 UT on 7 September 2017, 06:00–07:00 UT on 8 September 2017, and near 15:00UT on 8 September 2017, while ML-AIM did not show such rapid Φ_{PC} variations. Throughout this storm, the SuperDARN potential model tends to give the lowest Φ_{PC} predictions, the Weimer (2005) model is the highest, and the ML-AIM model Φ_{PC} values are between

10.1029/2023SW003683

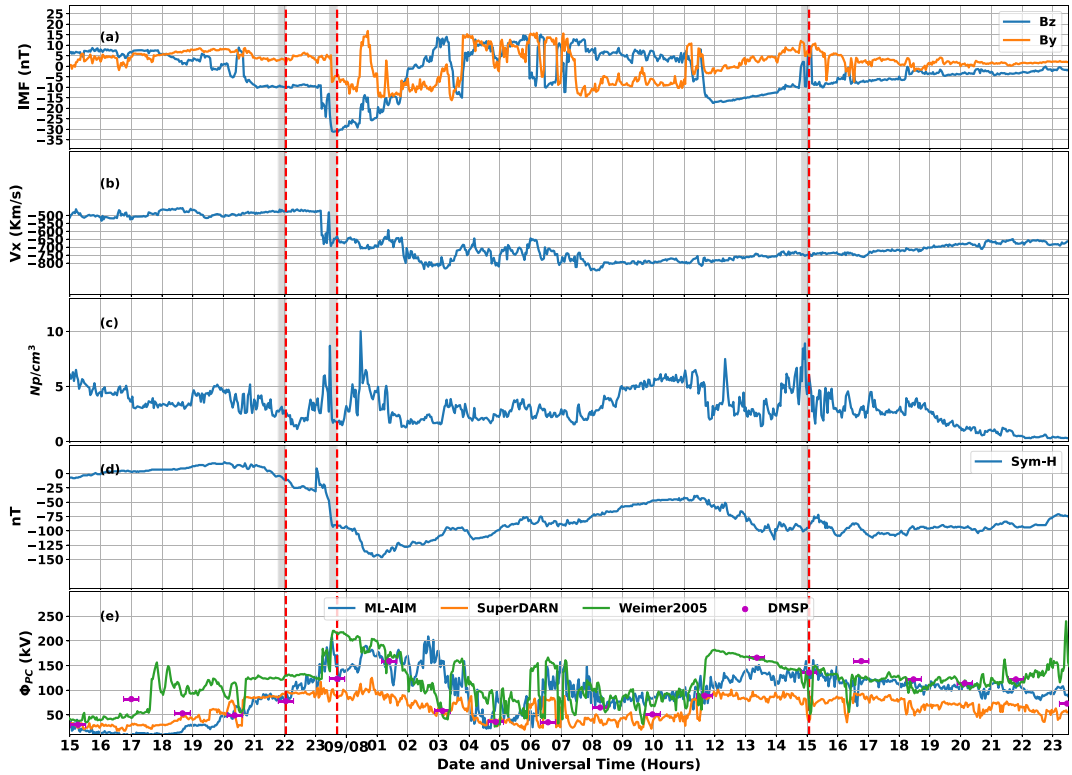

Figure 4. (a) IMF (b) solar wind velocity in Geocentric Solar Magnetospheric coordinates, (c) number density and (d) SYM-H, obtained from NASA OMNI data during 7–8 September 2017. The bottom panel (e) shows Φ_{PC} in the northern hemisphere as predicted by our ML-AIM (blue), Weimer (2005) model (green), and SuperDARN (orange). Magenta circles indicate the Φ_{PC} calculated from each polar crossing of Defense Meteorological Satellite Program F17 during 7–8 September 2017. The vertical dashed lines and shaded arears represent three case studies during (left to right) prolonged negative IMF Bz, minimum IMF Bz and sudden change in the IMF orientation from negative to positive, respectively (See text for more information).

the two. The low Φ_{PC} values of the SuperDARN model are understandable because its base model is from Thomas and Shepherd (2018) which utilized the SuperDARN data during the uniquely quiet solar cycle 24. Therefore, the SuperDARN potential model has limitations to predict the potential pattern for the solar electric field greater than 3 mV/m (Orr et al., 2023).

To compare model predictions of global ionospheric potentials, we selected three incidents (vertical dashed lines in Figure 4) at 22:02 UT on 7 September 2017 during prolonged southward IMF Bz, 23:42 UT on 7 September 2017 during the period of maximum southward IMF Bz, and 15:04 UT on 8 September 2017 during a period of sudden change of IMF Bz orientation. DMSP F 17 also crossed the northern hemisphere during the three incidents, providing the data set for model-data comparison. The SW/IMF and geomagnetic conditions used to compute potentials are highlighted with vertical dashed lines and shaded areas (60-min time history) in Figure 4.

Figure 5 shows the ionospheric potential patterns of the northern hemisphere predicted by ML-AIM (left), Weimer (2005) (middle), and SuperDARN (right) for the three incidents at 22:02 UT on 7 September 2017 during prolonged southward IMF Bz, 23:42 UT (top) on 7 September 2017 during the period of maximum southward IMF Bz (middle), and 15:04 UT on 8 September 2017 during a period of sudden change of IMF Bz orientation (bottom). Noon is located at the top of each plot. The dashed lines represent 3-hr MLT grids and 5°-MLAT grids. Φ_{PC} of each plot is displayed at the bottom. The magenta lines indicate the plasma convection velocities observed by the DMSP F17 when it crossed the northern polar region. The DMSP Φ_{PC} is calculated during each polar crossing and displayed with magenta in the upper right corners of Figures 5a, 5d, and 5g. The green dots in Figures 5c, 5f, and 5i represent the locations of SuperDARN radar measurements used for deriving the ionospheric potential maps.

10.1029/2023SW003683

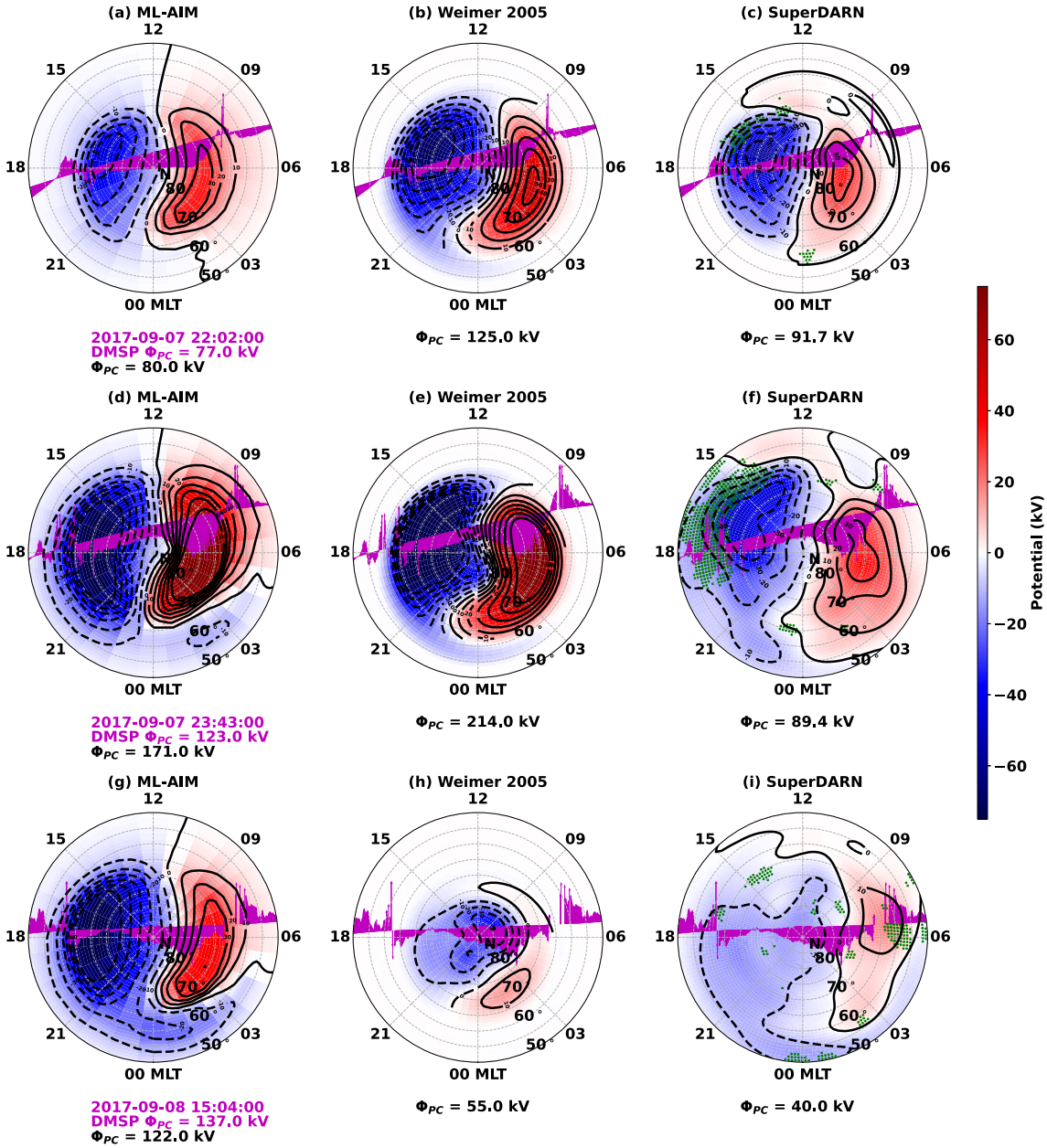

Figure 5. Magnetic local time (MLT) and Magnetic Latitude maps of ionospheric potentials obtained from the ML-AIM (left), Weimer (2005) (middle), and SuperDARN (right) at 22:02 UT on 7 September 2017 (top), 23:42 UT on 7 September 2017 (middle), and 15:04 UT on 8 September 2017 (bottom). The noon is located at the top of each plot. The dashed lines indicate 3-hr MLT and 5°-MLAT grids. Φ_{PC} of each plot is indicated in the bottom of each plot. The plasma convection velocities and Φ_{PC} obtained from Defense Meteorological Satellite Program 17 are displayed in magenta. The green circles in SuperDARN maps represent the locations of radar measurements used for deriving the potential pattern.

Figure 5a shows the two-cell convection pattern with maximum potential in the dawn sector and minimum potential in the dusk sector. The Φ_{PC} from DMSP and ML-AIM are comparable during this steady IMF Bz condition. Similar potential patterns are predicted by the Weimer (2005) (Figure 5b) and SuperDARN (Figure 5c) models. However, Weimer (2005) shows a higher Φ_{PC} than ML-AIM and SuperDARN. Note that SuperDARN radar observations are almost absent at this time and thus its potential pattern is strongly dependent on the statistical model of Thomas and Shepherd (2018). Figures 5d–5f show the potential maps at 23:42 UT during the period of maximum southward IMF Bz. The ML-AIM (Figure 5d) predicted strong enhancements of ionospheric potential and equatorward expansion of the two-cell potential structures, compared to the potential pattern in

Figure 5a. The Weimer model (Figure 5e) also showed a similar potential response. The ML-AIM Φ_{PC} is 171 kV, whereas the DMSP Φ_{PC} is 123 kV. However, the Weimer Φ_{PC} is significantly higher than the DMPS Φ_{PC}, while the SuperDARN Φ_{PC} is much lower. The horizontal velocities in the cases presented in Figure 5 have large discrepancies with the minimum (maximum) potentials and the velocity reversal. All models presented in this study do not show the expected velocity reversal during the geomagnetic storm of 7–8 September 2017 when compared with the DMSP horizontal plasma flow measurements. The locations of velocity reversal from DMSP observations and the location of minimum (maximum) potentials are off about 5° MLAT, which requires detailed investigation in future studies. Figures 5g–5i, show the potential maps at 15:04 UT on 8 September 2017 when IMF Bz fluctuates and Φ_{PC} rapidly drops for a short period of time (see Figure 4e). The ML-AIM showed an enhanced potential pattern compared to the one in Figure 5a. Subsequently, its Φ_{PC} significantly increases, similar to the DMSP Φ_{PC}. On the other hand, the Weimer (2005) and SuperDARN Φ_{PC} severely underestimated Φ_{PC} compared to the ML-AIM and DMSP Φ_{PC} values. This study shows that ML-AIM reproduces overall storm-time responses of ionospheric electric potentials.

Identifying the most effective parameter for validating a global model like ML-AIM is challenging. The CPCP (Φ_{PC}) is one of the parameters used for quantifying auroral electrodynamics model's performance (e.g., Connor et al., 2014; Orr et al., 2023). Following these works, we adopt a similar approach for the ML-AIM validation. We considered DMSP-derived Φ_{PC} values as ground truth for model comparison, but with caution because of the observational limitation. As previously mentioned, DMSP takes roughly 20–25 min to cross the polar cap, and the global ionospheric potential pattern continuously vary during this period. Therefore, the derived DMSP Φ_{PC} may include a large error, especially during active times. Additionally, the DMSP F17 orbit may miss real maximum/minimum potential regions in the northern ionosphere, leading to an underestimation of Φ_{PC}. Nevertheless, the Φ_{PC} from DMSP can provide close approximations of observed ionospheric convections and be comparable to the Φ_{PC} from a global model. Therefore, we considered DMSP observations as a ground truth for the quantitative assessment of ML-AIM's ionospheric convection.

We evaluated the model performance by utilizing the 2017 data from DMSP F17. A total of 3204 DMSP F17 polar crossings were identified and the corresponding Φ_{PC} were computed using the methodology explained in Section 3. The choice of the year 2017 is deliberate as it falls outside the training set for the CNN-FAC model. Additionally, the geomagnetic active days utilized for the Robinson et al. (2020) conductance model database does not include data from 2017. Hence, this year is deemed most suitable for model assessment.

Figure 6 shows the comparison between Φ_{PC} from DMSP polar crossings of the year 2017 and Φ_{PC} from ML-AIM (blue), Weimer (2005) (green), and SuperDARN (orange). The corresponding linear fits are also shown with the same color. The Root Mean Squared Error (RMSE), Mean Absolute Error (MAE), and Correlation Coefficient are also mentioned with the same color code. The RMSEs are 24, 28, and 27 keV for ML-AIM, Weimer (2005) and SuperDARN, respectively. The MAE are 18, 22, and 19 keV for ML-AIM, Weimer (2005) and SuperDARN. The correlation coefficients between modeled and measured Φ_{PC} are 0.45, 0.39, and 0.37 for the ML-AIM, Weimer (2005) and SuperDARN, respectively. Note that all the models presented here are still underestimating Φ_{PC} when compared to the DMSP observations. This is understandable considering the caveat of statistical models that average out the dynamic events as well as the observational constraints for the DMSP Φ_{PC} measurements. From Figure 6, one can clearly notice that the ML-AIM showed better performance in terms of RMSE, MAE, and correlation coefficient values when compared to the Weimer (2005) and SuperDARN-based models.

Similarly, Figure 7 shows the means (colored circles) and standard deviations (error bars) of Φ_{PC} values from DMSP observations (black), ML-AIM (blue), Weimer (2005) (green), and SuperDARN (orange) as a function of the Kp-index. The total number of DMSP polar crossings for a given Kp-index level is indicated with gray bars in the background. The mean Φ_{PC} values from ML-AIM closely match the mean Φ_{PC} of DMSP observations for most of the Kp-index values. The mean Φ_{PC} predicted by Weimer (2005) is slightly above the mean values of DMSP observations, whereas the SuperDARN Φ_{PC} is below the mean values of DMSP observations. Another interesting observation from Figure 7 is that the upper limit of the standard deviation bars of Weimer (2005) is above the upper limit of the standard deviation of DMSP observations for most Kp indices, indicating the overall overestimation of Weimer (2005). On the other hand, the lower limit of the standard deviation of SuperDARN tends to go below the standard deviation of DMSP observations for Kp > 3, indicating the underestimation of Φ_{PC} for moderately and strongly active times. In the case of ML-AIM, both upper and lower limits are within the

10.1029/2023SW003683

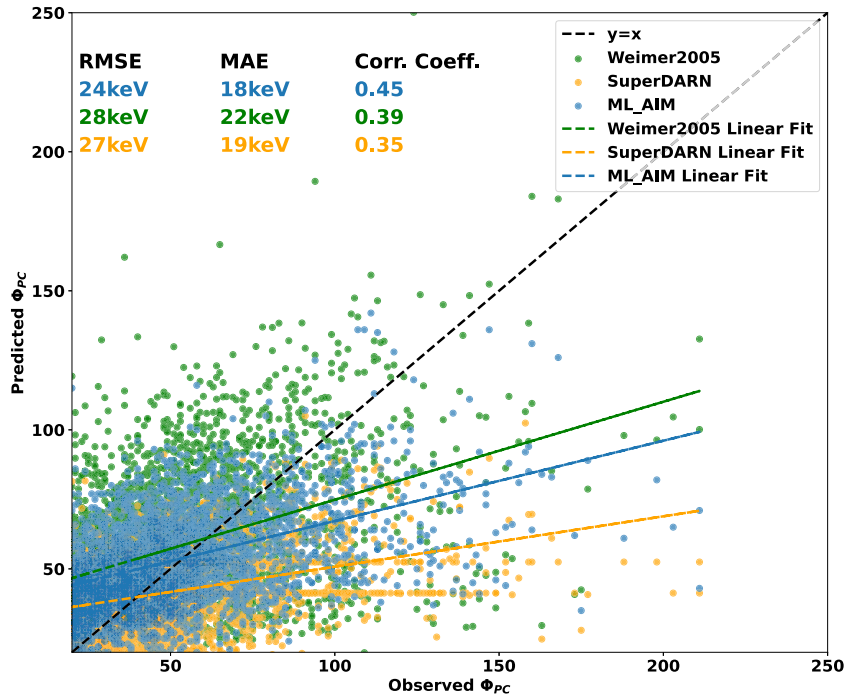

Figure 6. Comparison between Cross Polar Cap Potentials (CPCP; Φ_{PC}) from Defense Meteorological Satellite Program polar crossings of the year 2017 and predicted values from ML-AIM (blue), Weimer (2005) (green), and SuperDARN (orange). The corresponding linear fits are also shown with the same color. The Root Mean Squared Error, Mean Absolute Error, and Correlation Coefficient are also mentioned with the same color code.

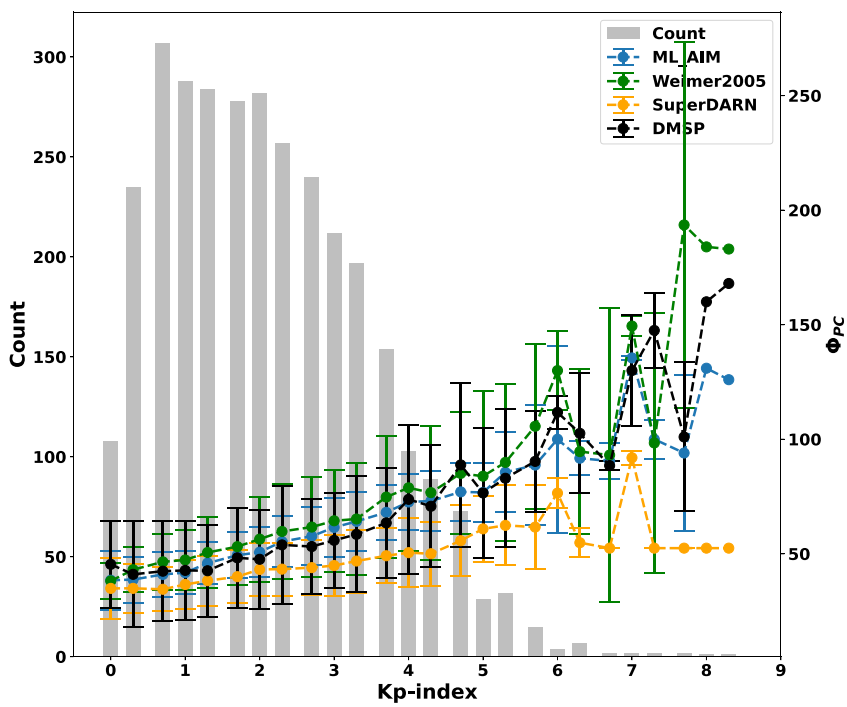

Figure 7. Means (colored circles) and standard deviations (error bars) of Cross Polar Cap Potential (Φ_{PC}) values from Defense Meteorological Satellite Program observations (black), ML-AIM (blue), Weimer (2005) (green), SuperDARN (orange) as a function of the Kp-index. The number of data points for a given Kp-index level are indicated with gray bars.

standard deviation of DMSP Φ_{PC} observations for all Kp values, except Kp > 6 where the standard deviation becomes non-meaningful due to the lack of cases.

The quantitative assessment presented in Figures 6 and 7 reveals that all models, including ML-AIM, underestimated Φ_{PC} compared to DMSP observations. However, Figure 6 suggests that ML-AIM showed better performance in terms of RMSE, MAE, and correlation coefficient values when compared to Weimer (2005) and SuperDARN. Notably, the mean Φ_{PC} values from ML-AIM (Figure 7) closely aligned with DMSP observations across different Kp-index levels, suggesting a better prediction compared to other models.

5. Discussion

The characterization of the auroral electrodynamics is crucial for specifying the magnetospheric forcing in the GCMs. In this study, we demonstrated that the auroral electrodynamics can be derived by using the pre-trained ML-models. First, we generated the FACs (using CNN-FAC) and then FAC-driven conductances in the framework with the 60-min time history of SW/IMF and geomagnetic indices as the primary inputs. Later, we computed the convection potential, and all other ionospheric electrodynamics parameters over the auroral region by solving a current continuity equation. The spatial resolution of the ML-AIM is 1° MLAT × 1 hr MLT and the temporal resolution can be down to 2 min by sliding the 60-min input window by 2 min. The ML-AIM presented in this study has shown a promising performance under weak and strong geomagnetic activity. During the periods when IMF Bz turns its sign abruptly (e.g., 20:30 UT on 7 September 2017 and 15:04 UT on 8 September 2017), the ML-AIM showed a slowly increasing Φ_{PC} while both Weimer (2005) and SuperDARN models showed rapid enhancement. The latter models are designed to provide the most probable ionospheric convection pattern when the given solar wind and IMF conditions stay constant. They are not designed to capture the gradual ionospheric response to the time-varying solar wind/IMF conditions. Due to this caveat, these models predict the immediate response of the ionosphere potential pattern to the sudden SW/IMF changes without allowing time for the ionosphere to re-adjust. It is unlikely that an entire ionospheric potential pattern gets modified within a couple of minutes after the SW/IMF change, causing an immediate Φ_{PC} enhancement (e.g., Figures 5h and 5i during a short excursion to a northward IMF). On the other hand, our ML-AIM model considers slow adjustment of the ionosphere to some extent by predicting ionospheric electrodynamics based on the 60-min time history of solar wind/IMF and geomagnetic indices. Therefore, we can faithfully conclude that our model provides more realistic potential patterns than the statistical empirical models.

From the validation studies (Figure 6), it is evident that all models, including ML-AIM, underestimated the Φ_{PC} when compared to the DMSP observation from 2017 (Figure 6). The Weimer (2005) is a statistical model, which is designed to provide the average state of the ionospheric convection under steady solar wind/IMF conditions using limited observations of DE-2 spacecraft between August 1981 and March 1983. The SuperDARN potentials often face the data coverage problem. When the SuperDARN observations are very limited, the output will converge to the statistical convection model of Thomas and Shepherd (2018). Further, high frequency radars systematically underestimate ionospheric potentials because the ionospheric refractive index is lower than the assumed unity.

The base models used for ML-AIM have some limitations that are worth mentioning here. As noted by Kunduri et al. (2020), the CNN-FAC model performs well under the low-to-moderate geomagnetic conditions. The comparison between bin-averaged statistical model and the CNN-FAC revealed that the CNN-FAC exhibits diminished predictive accuracy during high geomagnetic activity. The underestimation of CNN-FAC during moderate to strong geomagnetic conditions result in the underestimation of the ML-AIM potentials. Figure 6 illustrates this behavior, showing underestimated ML-AIM Φ_{PC} values when compared to DMSP observations. Since ML-AIM outputs are largely influenced by CNN-FAC, the model performance is expected to diminish during strong geomagnetic conditions. The ML-AIM expected to perform better under the low-to-moderate geomagnetic conditions. The CNN-FAC model was trained from the AMPERE FAC data during 2010–2016 (Kunduri et al., 2020). Only a few geomagnetic storms exist in this period and thus the CNN-FAC model is likely biased toward the quiet times, limiting the ML-AIM performance during strong geomagnetic times. Recently, AMPERE expanded its database with data from the new iridium-next satellite constellation, and with this updated data set, FAC estimation in ML-AIM can be further improved. Another source of error for the ML-AIM output is the conductance estimation from Robinson et al. (2020). It is worth mentioning here that the Pedersen conductivity in the upward FAC is comparable to that in the downward FAC (Figure 2b). The

comparable conductance between upward and downward FAC regions is due to the stronger downward FACs and/or the MLT sectors. ML-AIM adopts the conductance model of Robinson et al. (2020). Their paper derived various FAC-vs-conductance relations at eight different MLT sectors by utilizing simultaneous observations of AMPERE FACs and PFISR conductances for 20 geomagnetically active days. Their statistical analysis reveals that Pedersen conductance is generally stronger in the upward FAC region. However, Pedersen conductance in the downward FAC region can be as large as or even higher than the one in upward FAC region if downward FACs are comparable to or stronger than upward FACs in a certain MLT sector. This FAC-conductance relation of Robinson et al. (2020) should be used with caution because their relations are established for ∼65° MLAT (the PFISR MLAT), using only 20 days of observation. Additionally, the conductance maps are influenced by the performance of the CNN-FAC model, thus limiting the overall model performance of ML-AIM during strong geomagnetic conditions. Furthermore, ML-AIM neglects neutral wind contribution when solving the ionospheric electrodynamics with Ohm's law. Neutral winds typically increase during a geomagnetic storm and can introduce larger errors in the ML-AIM results. Lastly, the AMPERE database used in the CNN-FAC model has its own bias and conversion limitations (Anderson et al., 2014) that are impossible to avoid unless new techniques are introduced for the FAC derivation. Considering these limitations of base models, ML-AIM outputs should be used with caution during strong geomagnetic activity (for e.g. Kp > 6).

Apart from these intrinsic limitations, the CNN-FAC model is developed for the northern hemisphere (Kunduri et al., 2020), limiting the ML-AIM ability to predict the ionospheric electrodynamics in the southern hemisphere. However, Hatch et al. (2022) reported that on average, the northern and southern hemisphere are quite symmetrical if the sign of IMF By and the dipole tilt angle are adjusted for the south. Exploration of different methodologies for adjusting the model results to southern hemisphere will be explored in future studies.

In conclusion, ML-AIM reproduces physically accurate ionospheric electrodynamics patterns for the two selected events of southward IMF turning and a geomagnetic storm. ML-AIM also provides better statistical performance in determining the cross polar cap potentials than the Weimer (2005) and SuperDARN models compared to CPCP values derived from DMSP cross-track measurements. Therefore, the current ML-AIM version successfully lays the groundwork for an ML-based space weather prediction model that integrates various ML-models in the magnetosphere-ionosphere-thermosphere system under a single framework for accurately predicting the space weather-relevant quantities.

6. Summary and Future Work

This study introduces a ML based Auroral Ionosphere electrodynamics Model (ML-AIM) that solves a current continuity equation with the CNN FAC model of Kunduri et al. (2020) and the statistical conductance models of Moen and Brekke (1993) and Robinson et al. (2020). The ML-AIM inputs are 60-min time histories of three IMF components (B_x, B_y, and B_z), solar wind velocity (V_x), proton number density (N_p), geomagnetic indices (Sym-H, Asym-H, SuperMAG AL, and AU indices), F10.7 solar flux, and the month number. By sliding the 60-min input window by 1 min, ML-AIM produces electrostatic potential, electric field, Joule heating rate, and horizontal ionospheric currents every minute. We conducted two event studies of a weak geomagnetic event on 14 May 2013 and a geomagnetic storm on 7–8 September 2017. ML-AIM reproduced the well-known two-cell convection pattern for southward IMF and its expansion to lower latitudes for stronger southward IMF. It's overall Φ_{PC} responses to the time-varying solar wind/IMF conditions are reasonable and comparable to the DMSP observations and the ones of Weimer (2005) and SuperDARN models. We validated the Φ_{PC} values predicted by ML-AIM with the DMSP F17 data from 2017. We found that ML-AIM model showed better performance in terms of RMSE, MAE, and correlation coefficient values compared to both the Weimer (2005) and SuperDARN-based models.

However, there is a notable difference in the Φ_{PC} predictions between models during rapid IMF changes (e.g., sudden southward IMF turnings at ∼06:40 UT on 14 May 2013 and ∼11:30 UT on 8 September 2017; brief IMF Bz fluctuations at ∼20:30 UT on 7 September 2017, 06:00–07:00 UT on 8 September 2017, and ∼15:00 UT on 8 September 2017). The Weimer (2005) and SuperDARN models abruptly changed the entire ionospheric potential maps without time to re-adjust the ionosphere for the new upstream conditions and thus immediately increase Φ_{PC}. This is understandable since the empirical models are designed to predict a static ionosphere for steady solar wind/IMF conditions. On the other hand, ML-AIM showed slower responses of electric potentials and Φ_{PC} to the rough IMF changes. This is because ML-AIM uses 60 min time histories of SW/IMF and geomagnetic conditions

as input and thus predicts ionospheric responses to the time-varying upstream conditions. Thus, ML-AIM is unique and better suited for forecasting high-latitude electrodynamics than the other empirical models, especially during a dynamic space weather event. ML-AIM can also provide more realistic ionospheric electric potentials as input for a general circulation model like GITM, Thermosphere Ionosphere Electrodynamics General Circulation Model, and Whole Atmosphere Community Climate Model with thermosphere and ionosphere extension, improving our understanding of the global ionosphere–thermosphere dynamics.

In the future, we will improve the ML-AIM by adding more advanced ML-based M-I-T models. First, we will update the CNN-FAC model with AMPERE-next (2017-present) data sets, which can significantly improve the FAC estimation in ML-AIM. This can potentially address the underestimation of FAC during moderate to large geomagnetic activity in ML-AIM framework. Second, we will update the ionospheric conductance model using the ML-based particle precipitation models. As discussed, the auroral conductance estimation in the present ML-AIM needs significant improvements. The auroral conductance can be derived using the total energy flux and mean energy of precipitating electrons by Robinson et al. (1987) formula. The conductance can also be estimated from an energy spectrum of auroral precipitation using the methods described in Fang et al. (2008, 2013). Currently, we are also developing the ML-based particle precipitation model with the DMSP and NASA OMNI data sets for predicting the electron/ion differential energy spectra in the 30 eV–30 keV energy band based on the time history of the solar wind conditions and geomagnetic indices without making assumptions about the specific shape of the spectra. This model can significantly improve the conductance estimation compared to the previous methods (Robinson et al., 1987, 2020). We will explore these techniques for improving the auroral conductance in ML-AIM framework. Third, we will calculate the ground magnetic field using the horizontal ionospheric currents with 1-min time resolution and the ground magnetic field perturbations. The magnetic field perturbations will be compared with the SuperMAG observations for a better understanding of the ML-AIM response under varying SW/IMF conditions. Further, we will calculate the potential regions of high GIC risks using the magnetic field perturbation maps generated by the ML-AIM.

Data Availability Statement

The SuperDARN fitted potentials are openly available from the Center for Space Science and Engineering Research, Virginia Tech (SuperDARN, 2024). The Weimer (2005) model Run-on-request results are published by CCMC (2024). DMSP ion drift data are available from Cornell open madrigal (Cornell Open Madrigal, 2024). The IMF, solar wind, and geomagnetic indices data are available from the NASA Space Physics Data Facility OMNIWeb data server (OMNIWeb, 2024). The CNN-FAC model is available in Kunduri (2020). The ML-AIM outputs have been posted on Zenodo (Sai Gowtam et al., 2024).

Acknowledgments
The work of VSG is supported by National Science Foundation Grant GIC EPSCoR 367841/66758. The authors acknowledge use of NASA/GSFC's Space Physics Data Facility's OMNIWeb service, and OMNI data (https://omniweb.gsfc.nasa.gov/form/omni_min.html). HKC gratefully acknowledges support of the NASA GSFC internal funding programs (HIF, ISFM, and IRAD). DMSP ion drift data are openly available at http://landau.geo.cornell.edu/madrigal/index.html/. BSRK acknowledges support from the National Science Foundation under Grant AGS-1839509 and NASA for support under Grants 80NSSC22K1635 and 80NSSC23K1321. The authors acknowledge the use of SuperDARN data (http://vt.superdarn.org/). SuperDARN is a collection of radars funded by national scientific funding agencies of Australia, Canada, China, France, Italy, Japan, Norway, South Africa, United Kingdom, and the United States of America. The Weimer (2005) model results have been provided by the Community Coordinated Modeling Center at Goddard Space Flight Center through their publicly available simulation services (https://ccmc.gsfc.nasa.gov). Authors also acknowledge the open-source SuperDARN Python software (pyDARN) (https://zenodo.org/record/3727270#.YypfTXbMJD8). Most of the analysis and visualization were completed with the help of free, open-source Python software tools such as matplotlib (Hunter, 2007), IPython (Pérez & Granger, 2007), Pandas (McKinney, 2010), TensorFlow (Abadi et al., 2015) and others (Millman & Aivazis, 2011).

References

Abadi, M., Agarwal, A., Barham, P., Brevdo, E., Chen, Z., Citro, C., et al. (2015). TensorFlow: Large-scale machine learning on heterogeneous systems [Software]. Retrieved from https://www.tensorflow.org/

Anderson, B. J., Korth, H., Waters, C. L., Green, D. L., Merkin, V. G., Barnes, R. J., & Dyrud, L. P. (2014). Development of large-scale Birkeland currents determined from the active magnetosphere and planetary electrodynamics response experiment. *Geophysical Research Letters*, *41*(9), 3017–3025. https://doi.org/10.1002/2014GL059941

Anderson, B. J., Takahashi, K., Kamei, T., Waters, C. L., & Toth, B. A. (2002). Birkeland current system key parameters derived from Iridium observations: Method and initial validation results. *Journal of Geophysical Research*, *107*(A6), SMP11-1–SMP11-13. https://doi.org/10.1029/2001JA000080

Anderson, B. J., Takahashi, K., & Toth, B. A. (2000). Sensing global Birkeland currents with Iridium® engineering magnetometer data. *Geophysical Research Letters*, *27*(24), 4045–4048. https://doi.org/10.1029/2000gl000094

Birkeland, K. (1901). *Résultats des rescherches magnéthiques faites par l'expédition Norvégienne de 1899–1900* (pp. 565–586). Archives des Sciences Physiques et Naturelles.

Blanc, M., & Richmond, A. D. (1980). The ionospheric disturbance dynamo. *Journal of Geophysical Research*, *85*(A4), 1669–1688. https://doi.org/10.1029/ja085ia04p01669

Blandin, M., Connor, H. K., Öztürk, D. S., Keesee, A. M., Pinto, V., Mahmud, M. S., et al. (2022). Multi-variate LSTM prediction of Alaska magnetometer chain utilizing a coupled model approach. *Frontiers in Astronomy and Space Sciences*, *9*, 846291. https://doi.org/10.3389/fspas.2022.846291

Boudouridis, A., Zesta, E., Lyons, L. R., Anderson, P. C., & Lummerzheim, D. (2005). Enhanced solar wind geoeffectiveness after a sudden increase in dynamic pressure during southward IMF orientation. *Journal of Geophysical Research*, *110*(A5), A05214. https://doi.org/10.1029/2004JA010704

Bristow, W. A., Topliff, C. A., & Cohen, M. B. (2022). Development of a high-latitude convection model by application of machine learning to SuperDARN observations. *Space Weather*, *20*(1), e2021SW002920. https://doi.org/10.1029/2021SW002920

CCMC. (2024). Community coordinated modeling center [Dataset]. *NASA Goddard Space Flight Center*. Retrieved from https://ccmc.gsfc.nasa.gov/ungrouped/IT/Iono_main.php

Connor, H. K., Zesta, E., Fedrizzi, M., Shi, Y., Raeder, J., Codrescu, M. V., & Fuller-Rowell, T. J. (2016). The ionosphere-thermosphere response to a geomagnetic storm using physics-based magnetospheric energy input: OpenGGCM-CTIM results. *Journal of Space Weather and Space Climate*, *6*, A25. https://doi.org/10.1051/swsc/2016019

Connor, H. K., Zesta, E., Ober, D. M., & Raeder, J. (2014). The relation between transpolar potential and reconnection rates during sudden enhancement of solar wind dynamic pressure: OpenGGCM-CTIM results. *Journal of Geophysical Research: Space Physics*, *119*(5), 3411–3429. https://doi.org/10.1002/2013JA019728

Cornell Open Madrigal. (2024). Cornell open madrigal [Dataset]. Retrieved from http://landau.geo.cornell.edu/madrigal/index.html/

Cousins, E. D. P., Matsuo, T., & Richmond, A. D. (2013). SuperDARN assimilative mapping. *Journal of Geophysical Research: Space Physics*, *118*(12), 7954–7962. https://doi.org/10.1002/2013JA019321

Cousins, E. D. P., & Shepherd, S. G. (2010). A dynamical model of high-latitude convection derived from SuperDARN plasma drift measurements. *Journal of Geophysical Research*, *115*(A12), A12329. https://doi.org/10.1029/2010JA016017

Dungey, J. W. (1961). Interplanetary magnetic field and the auroral zones. *Physical Review Letters*, *6*(2), 47–48. https://doi.org/10.1103/PhysRevLett.6.47

Fang, X., Lummerzheim, D., & Jackman, C. H. (2013). Proton impact ionization and a fast calculation method. *Journal of Geophysical Research: Space Physics*, *118*(8), 5369–5378. https://doi.org/10.1002/jgra.50484

Fang, X., Randall, C. E., Lummerzheim, D., Solomon, S. C., Mills, M. J., Marsh, D. R., et al. (2008). Electron impact ionization: A new parameterization for 100 eV to 1 MeV electrons. *Journal of Geophysical Research*, *113*(A9), A09311. https://doi.org/10.1029/2008JA013384

Fuller-Rowell, T. J., & Evans, D. S. (1987). Height-integrated Pedersen and Hall conductivity patterns inferred from the TIROS-NOAA satellite data. *Journal of Geophysical Research*, *92*(A7), 7606–7618. https://doi.org/10.1029/JA092iA07p07606

Fuller-Rowell, T. J., Rees, D., Quegan, S., Moffett, R. J., Codrescu, M. V., & Millward, G. H. (1996). A coupled thermosphere-ionosphere model (CTIM). In R. W. Schunk (Ed.), *STEP: Handbook of ionospheric models* (pp. 217–238). Utah State University.

Goodman, M. L. (1995). A three-dimensional, iterative mapping procedure for the implementation of an ionosphere-magnetosphere anisotropic Ohm's law boundary condition in global magnetohydrodynamic simulations. *Annales Geophysicae*, *13*(8), 843. https://doi.org/10.1007/s005850050223

Gowtam, V. S., Tulasi Ram, S., Reinisch, B., & Prajapati, A. (2019). A new artificial neural network-based global three-dimensional ionospheric model (ANNIM-3D) using long-term ionospheric observations. *Preliminary Results*, *124*(6), 4639–4657. https://doi.org/10.1029/2019JA026540

Hardy, D. A., Gussenhoven, M. S., Raistrick, R., & McNeil, W. J. (1987). Statistical and functional representations of the pattern of auroral energy flux, number flux, and conductivity. *Journal of Geophysical Research*, *92*(A11), 12275–12294. https://doi.org/10.1029/JA092iA11p12275

Hatch, S. M., Laundal, K. M., & Reistad, J. P. (2022). Testing the mirror symmetry of Birkeland and ionospheric currents with respect to magnetic latitude, dipole tilt angle, and IMF By. *Frontiers in Astronomy and Space Sciences*, *9*, 958977. https://doi.org/10.3389/fspas.2022.958977

Heelis, R. A., Lowell, J. K., & Spiro, R. W. (1982). A model of the high-latitude ionospheric convection pattern. *Journal of Geophysical Research*, *87*(A8), 6339–6345. https://doi.org/10.1029/JA087iA08p06339

Hu, A., Shneider, C., Tiwari, A., & Camporeale, E. (2022). Probabilistic prediction of Dst storms one-day-ahead using full-disk SoHO images. *Space Weather*, *20*(8), e2022SW003064. https://doi.org/10.1029/2022SW003064

Hunter, J. D. (2007). Matplotlib: A 2D graphics environment. *Computing in Science & Engineering*, *9*(3), 90–95. https://doi.org/10.1109/MCSE.2007.55

Iijima, T., & Potemra, T. A. (1976). The amplitude distribution of field-aligned currents at northern high latitudes observed by Triad. *Journal of Geophysical Research*, *81*(13), 2165–2174. https://doi.org/10.1029/ja081i013p02165

Kunduri, B. (2020). Convolutional neural network-field aligned currents (CNN-FAC) model [Dataset]. https://zenodo.org/records/3872345#.Yyplp3bMJD8

Kunduri, B. S. R., Maimaiti, M., Baker, J. B. H., Ruohoniemi, J. M., Anderson, B. J., & Vines, S. K. (2020). A deep learning based approach for modeling the dynamics of AMPERE Birkeland currents. *Journal of Geophysical Research: Space Physics*, *125*(8), e2020JA027908. https://doi.org/10.1029/2020JA027908

Laundal, K. M., Finlay, C. C., Olsen, N., & Reistad, J. P. (2018). Solar wind and seasonal influence on ionospheric currents from Swarm and CHAMP measurements. *Journal of Geophysical Research: Space Physics*, *123*(5), 4402–4429. https://doi.org/10.1029/2018JA025387

Liu, E., Hu, H., Liu, J., & Qiao, L. (2020). Deep learning models for estimation of the SuperDARN cross polar cap potential. *Earth and Space Science*, *7*(8), e2020EA001219. https://doi.org/10.1029/2020EA001219

Lu, G., Emery, B. A., Rodger, A. S., Lester, M., Taylor, J. R., Evans, D. S., et al. (1996). High-latitude ionospheric electrodynamics as determined by the assimilative mapping of ionospheric electrodynamics procedure for the conjunctive SUNDIAL/ATLAS 1/GEM period of March 28–29, 1992. *Journal of Geophysical Research*, *101*(A12), 26697–26718. https://doi.org/10.1029/96JA00513

Matsuo, T., Kilcommons, L. M., Ruohoniemi, J. M., & Anderson, B. J. (2019). Assimilative mapping of geospace observations (AMGeO): Data science tools for collaborative geospace systems science. In *AGU fall meeting abstracts* (Vol. 2019, p. SM33A-01).

McGranaghan, R. M., Ziegler, J., Bloch, T., Hatch, S., Camporeale, E., Lynch, K., et al. (2021). Toward a next generation particle precipitation model: Mesoscale prediction through machine learning (a case study and framework for progress). *Space Weather*, *19*(6), e2020SW002684. https://doi.org/10.1029/2020SW002684

McKinney, W. (2010). Data structures for statistical computing in python. In S. van der Walt, & J. Millman (Eds.), *Proceedings of the 9th Python in science conference* (pp. 51–56). Conference SciPy.

Millman, K. J., & Aivazis, M. (2011). Python for scientists and engineers. *Computing in Science & Engineering*, *13*(2), 9–12. https://doi.org/10.1109/MCSE.2011.36

Moen, J., & Brekke, A. (1993). The solar flux influence on quiet time conductances in the auroral ionosphere. *Geophysical Research Letters*, *20*(10), 971–974. https://doi.org/10.1029/92GL02109

Newell, P. T., Liou, K., Zhang, Y., Sotirelis, T., Mitchell, L. J. E. J., & Mitchell, E. J. (2014). OVATION Prime-2013: Extension of auroral precipitation model to higher disturbance levels. *Space Weather*, *12*(6), 368–379. https://doi.org/10.1002/2014SW001056

Newell, P. T., Sotirelis, T., & Wing, S. (2009). Diffuse, monoenergetic, and broadband aurora: The global precipitation budget. *Journal of Geophysical Research*, *114*(A9), A09207. https://doi.org/10.1029/2009JA014326

OMNIWeb. (2024). High resolution OMNI (HRO) data set consisting of interspersed 1-min averaged ACE, wind, IMP 8 and geotail magnetic field and plasma data [Dataset]. Retrieved from https://omniweb.gsfc.nasa.gov/html/hro_interface.html

Orr, L., Grocott, A., Walach, M.-T., Chisham, G., Freeman, M. P., Lam, M. M., & Shore, R. M. (2023). A quantitative comparison of high latitude electric field models during a large geomagnetic storm. *Space Weather*, *21*(1), e2022SW003301. https://doi.org/10.1029/2022SW003301

Pérez, F., & Granger, B. E. (2007). IPython: A system for interactive scientific computing. *Computing in Science & Engineering*, *9*(3), 21–29. https://doi.org/10.1109/MCSE.2007.53

Pinto, V. A., Keesee, A. M., Coughlan, M., Mukundan, R., Johnson, J. W., Ngwira, C. M., & Connor, H. K. (2022). Revisiting the ground magnetic field perturbations challenge: A machine learning perspective. *Frontiers in Astronomy and Space Sciences*, *9*, 869740. https://doi.org/10.3389/fspas.2022.869740

Pirjola, R. (2005). Effects of space weather on high-latitude ground systems. *Advances in Space Research*, *36*(12), 2231–2240. https://doi.org/10.1016/j.asr.2003.04.074

Pulkkinen, A., & Engels, M. (2005). The role of 3-D geomagnetic induction in the determination of the ionospheric currents from the ground geomagnetic data. *Annales Geophysicae*, *23*(3), 909–917. https://doi.org/10.5194/angeo-23-909-2005

Pulkkinen, A., Rastätter, L., Kuznetsova, M., Singer, H., Balch, C., Weimer, D., et al. (2013). Community-wide validation of geospace model ground magnetic field perturbation predictions to support model transition to operations. *Space Weather*, *11*(6), 369–385. https://doi.org/10.1002/swe.20056

Raeder, J. (2003). Global magnetohydrodynamics-A tutorial. *Space Plasma Simulations*, 212–246.

Raeder, J., Berchem, J., & Ashour-Abdalla, M. (1998). The geospace environment modeling grand challenge: Results from a global geospace circulation model. *Journal of Geophysical Research*, *103*(A7), 14787–14797. https://doi.org/10.1029/98JA00014

Raeder, J., McPherron, R., Frank, L., Kokubun, S., Lu, G., Mukai, T., et al. (2001). Global simulation of the geospace environment modeling substorm challenge event. *Journal of Geophysical Research*, *106*(A1), 381–395. https://doi.org/10.1029/2000ja000605

Rastätter, L., Shim, J. S., Kuznetsova, M. M., Kilcommons, L. M., Knipp, D. J., Codrescu, M., et al. (2016). GEM-CEDAR challenge: Poynting flux at DMSP and modeled Joule heat. *Space Weather*, *14*(2), 113–135. https://doi.org/10.1002/2015SW001238

Rich, F., & Hairston, M. (1994). Large-scale convection patterns observed by DMSP. *Journal of Geophysical Research*, *99*(A3), 3827–3844. https://doi.org/10.1029/93JA03296

Richmond, A. D., & Kamide, Y. (1988). Mapping electrodynamic features of the high-latitude ionosphere from localized observations: Technique. *Journal of Geophysical Research*, *93*(A6), 5741–5759. https://doi.org/10.1029/ja093ia06p05741

Richmond, A. D., & Thayer, J. P. (2000). *Ionospheric electrodynamics: A tutorial* (pp. 131–146). American Geophysical Union (AGU). https://doi.org/10.1029/GM118p0131

Ridley, A. J., Deng, Y., & Tóth, G. (2006). The global ionosphere-thermosphere model. *Journal of Atmospheric and Solar-Terrestrial Physics*, *68*(8), 839–864. https://doi.org/10.1016/j.jastp.2006.01.008

Robinson, R. M., Kaeppler, S. R., Zanetti, L., Anderson, B. J., Vines, S. K., Korth, H., & Fitzmaurice, A. (2020). Statistical relations between auroral electrical conductances and field-aligned currents at high latitudes. *Journal of Geophysical Research: Space Physics*, *125*(7), e2020JA028008. https://doi.org/10.1029/2020ja02800

Robinson, R. M., Vondrak, R. R., Miller, K., Dabbs, T., & Hardy, D. (1987). On calculating ionospheric conductances from the flux and energy of precipitating electrons. *Journal of Geophysical Research*, *92*(A3), 2565–2569. https://doi.org/10.1029/ja092ia03p02565

Robinson, R. M., Zanetti, L., Anderson, B., Vines, S., & Gjerloev, J. (2021). Determination of auroral electrodynamic parameters from AMPERE field-aligned current measurements. *Space Weather*, *19*(4), e2020SW002677. https://doi.org/10.1029/2020SW002677

Roble, R. G., & Emery, B. A. (1983). On the global mean temperature of the thermosphere. *Planetary and Space Science*, *31*(6), 597–614. https://doi.org/10.1016/0032-0633(83)90002-8

Ruohoniemi, J. M., & Greenwald, R. A. (1996). Statistical patterns of high-latitude convection obtained from Goose Bay HF radar observations. *Journal of Geophysical Research*, *101*(A10), 21743–21763. https://doi.org/10.1029/96ja01584

Sai Gowtam, V., Connor, H., Kunduri, B. S. R., Raeder, J., Laundal, K. M., Tulasi Ram, S., et al. (2024). Calculating the high-latitude ionospheric electrodynamics using a machine learning-based field-aligned current model [Dataset]. https://zenodo.org/records/10688966

Sai Gowtam, V., & Tulasi Ram, S. (2017). An artificial neural network based ionospheric model to predict NmF2 and hmF2 using long-term data set of FORMOSAT-3/COSMIC radio occultation observations: Preliminary results. *Journal of Geophysical Research: Space Physics*, *122*(11), 11743–11755. https://doi.org/10.1002/2017JA024795

SuperDARN. (2024). Super dual auroral radar network [Dataset]. Retrieved from http://vt.superdarn.org/

Thomas, E. G., & Shepherd, S. G. (2018). Statistical patterns of ionospheric convection derived from mid-latitude, high-latitude, and polar SuperDARN HF radar observations. *Journal of Geophysical Research: Space Physics*, *123*(4), 3196–3216. https://doi.org/10.1002/2018JA025280

Tulasi Ram, S., Sai Gowtam, V., Mitra, A., & Reinisch, B. (2018). The improved two-dimensional artificial neural network-based ionospheric model (ANNIM). *Journal of Geophysical Research: Space Physics*, *123*(7), 5807–5820. https://doi.org/10.1029/2018JA025559

Waters, C. L., Anderson, B. J., Green, D. L., Korth, H., Barnes, R. J., & Vanhamäki, H. (2020). Science data products for AMPERE. In M. Dunlop, & H. Lühr (Eds.), *Ionospheric multi-spacecraft analysis tools*, *ISSI scientific report series* (Vol. 17). Springer. https://doi.org/10.1007/978-3-030-26732-2_7

Weimer, D. R. (2005). Improved ionospheric electrodynamic models and application to calculating joule heating rates. *Journal of Geophysical Research*, *110*(A5), A05306. https://doi.org/10.1029/2004JA010884

Wolf, R. A. (1983). The quasi-static (Slow-Flow) region of the magnetosphere. In R. L. Carovillano, & J. M. Forbes (Eds.), *Solar-terrestrial physics* (pp. 303–368). D. Reidel. https://doi.org/10.1007/978-94-009-7194-3_14